

Supporting information

Large breathing of the MOF type MIL-47(V) upon mechanical pressure: A joint experimental-modelling exploration

Pascal G. Yot, Qintian Ma, Julien Haines, Qingyuan Yang, Aziz Ghoufi, Thomas Devic, Christian Serre, Gérard Férey, Chongli Zhong, Guillaume Maurin

1. Mercury intrusion

Mercury intrusion which is usually employed to determine the pore size distribution and porosity¹ has been successfully used to study the mechanical behavior of aero-gel² or more recently MOF materials³. Considering the pore size of MIL-47(V) (and pressure range explored by mercury intrusion ($P \leq 350$ MPa)) the non-wetting mercury cannot penetrate into the pores, hence the pressure increase induces an isostatic pressure on the crystallites. The volume of intruded mercury is then directly related to the volumetric strain corresponding to the compressibility of the material. The isostatic compression experiments were performed using a Hg porosimeter Micromeritics Autopore 9240 on outgassed (~6.5 Pa, 4 h) powdered MIL-47(V) samples. The pressure applied can vary from 0.1 to 350 MPa.

In the explored range of pressure, using the Washburn's law $P = -\frac{4\gamma\cos\theta}{d}$

with γ mercury surface tension and θ the contact angle of 0.485 N/m and 130° respectively, the pore diameters range in the interval [2×10⁷–420 Å]. Cumulative and incremental volumes of intruded mercury have been reported as a function of the applied pressure with the aim at determining the effective pore diameter corresponding to the increase of volume at 125 MPa and 85 MPa (Figure S1).

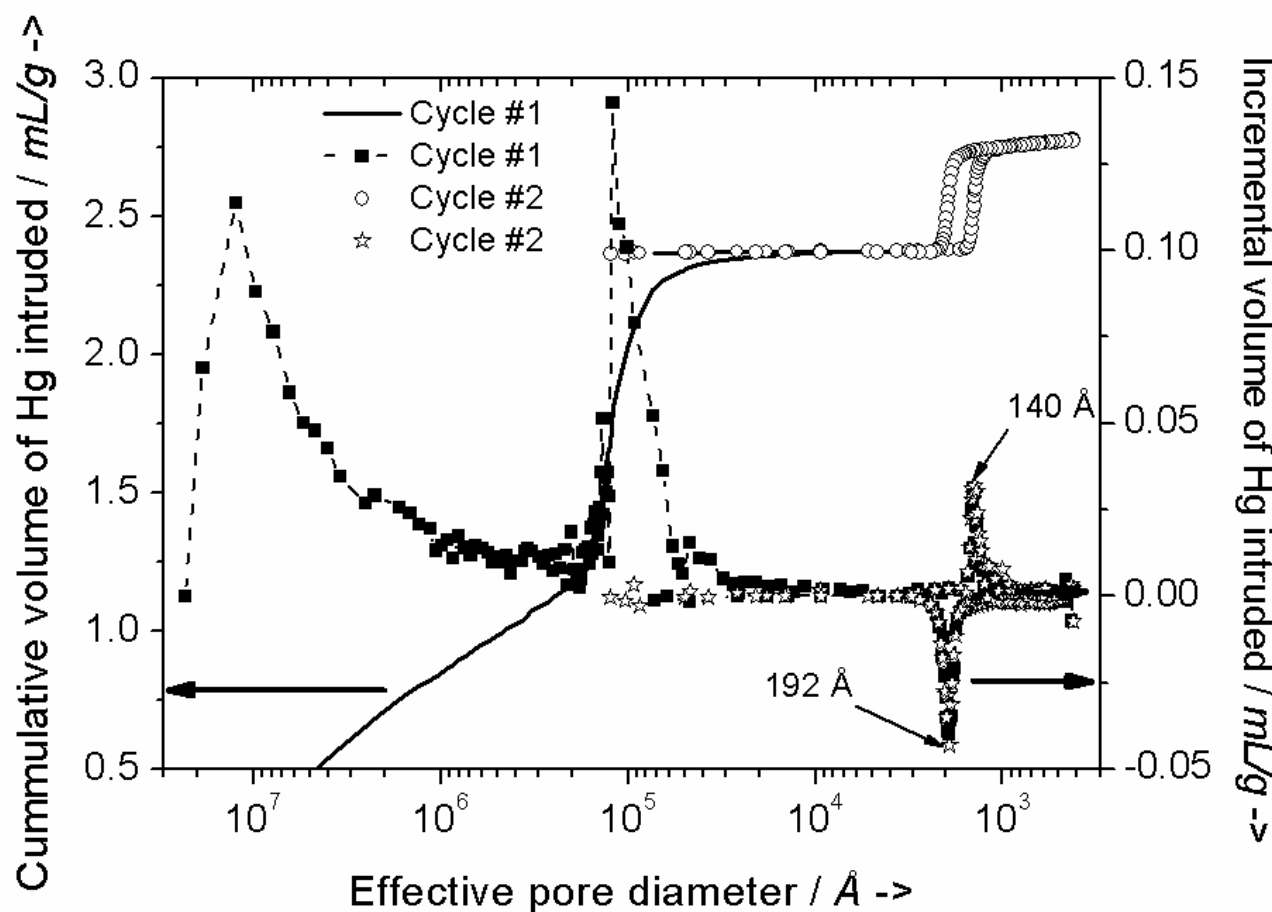


Figure S1 – Cumulative and incremental volumes of intruded mercury as a function of the effective pore diameter.

Volumes of mercury related to the steps obtained upon pressure increase and decrease correspond to pore diameters of 140 Å and 192 Å respectively that are much larger than the window size of the MIL-47(V). It confirms that the two steps observed on the mercury intrusion curves are only the result of the plastic deformation of the powder particles.

2. Pressure-induced Powder x-ray diffraction

Angle-dispersive X-ray diffraction data at high pressure was performed at the European Synchrotron Radiation Facility (ESRF, France) on the Swiss-Norwegian Beam Line (SNBL, BM01A) using a diamond anvil cell (DAC). The diffraction patterns were collected using MAR345 image plate detector, a monochromatic beam with the wavelength of 0.709622 Å and a time of exposition of 3 minutes. The sample to-detector distance (250 mm) and parameters of the detector

were calibrated using NIST standard LaB₆. Two-dimensional diffraction images were integrated using FIT2D software⁴. The pressures were generated by a DAC with flat culets of diameter 600 µm. The powder was loaded into a hole of 250 µm in diameter drilled in a stainless steel gasket pre-indented to 60-80 µm thickness; the beam was slit collimated to 140×140 µm². The pressures were measured from the shift of the ruby R1 fluorescence line⁷. Silicone oil (AP100, Fluka) was used with the aim at reaching good quasi-hydrostatic conditions. All the measurements were performed increasing and decreasing the pressure in the range 10⁻⁴-380 MPa. The unit-cell parameters were determined by indexing the X-Ray powder patterns, using DICVOL6 followed by a Le Bail fit using FULLPROF^{5,6}. Figures S2 and S3 present the results of Le Bail fits for the forms obtained at 0.1 and 178.1 MPa respectively.

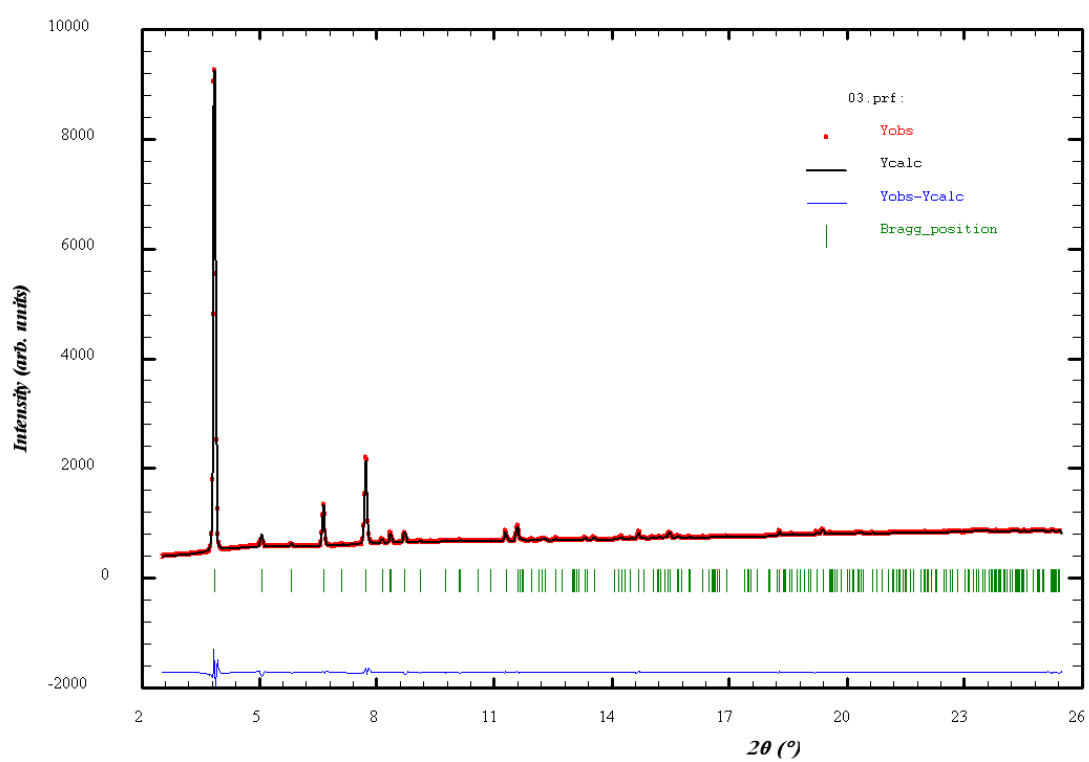


Figure S2 – Structure-independent refinements of the unit-cell of the diffraction pattern obtained at 0.1 MPa.

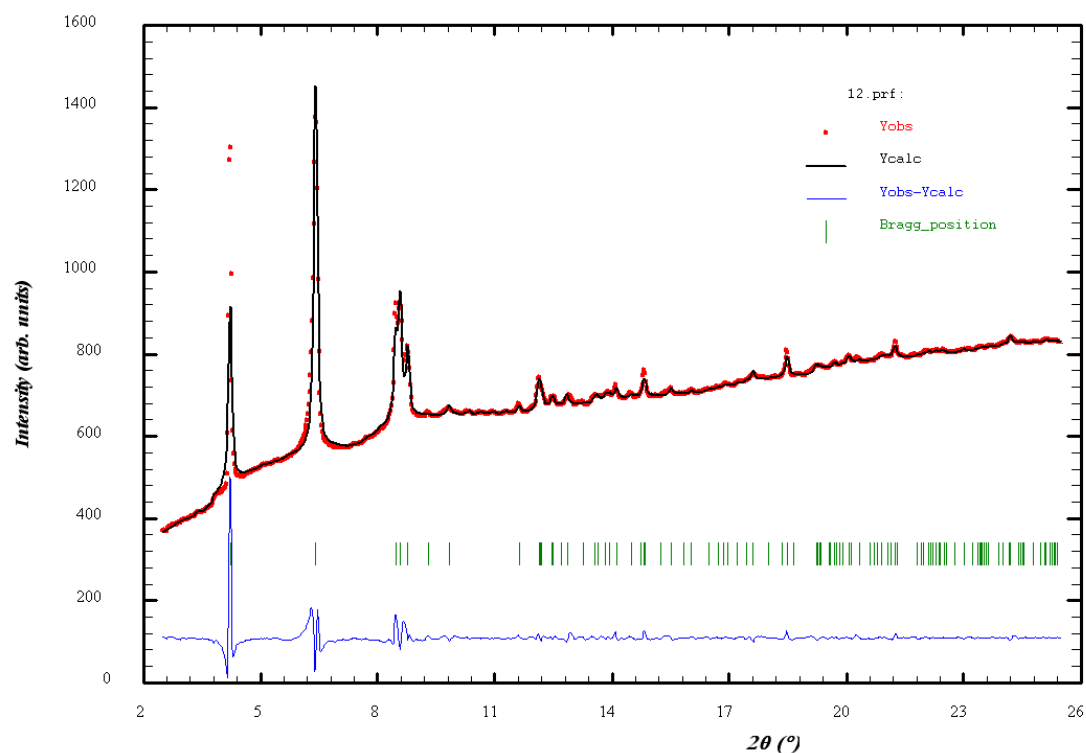


Figure S3 – Structure-independent refinements of the unit-cell of the diffraction pattern obtained at 178.1 MPa.

3. Micro-Raman scattering

Raman spectra were recorded using a Horiba Jobin-Yvon Labram Aramis spectrometer. The samples were placed under the $50\times$ or $100\times$ objectives of the Olympus microscope. 633 nm diode-laser with a power limited to $42\mu\text{W}$. The pressure generated with a DAC, was determined from the shift of the ruby R1 fluorescence line⁷. A steel gasket with a hole of 100 μm in diameter and pre-indented to 50 μm thickness where the powder was loaded has been used. At the difference of x-ray diffraction experiments, no transducer media was used to avoid overlapping sample and pressure transmitting media signals. Spectra were recorded in two regions $50\text{-}1300\text{ cm}^{-1}$ and $1400\text{-}2100\text{ cm}^{-1}$ with the aim at eliminating the Raman peak of the diamond used in the DAC to generate the pressure.

4. Details of molecular simulations

4.1. Charge distribution for the framework of MIL-47 (V) (Reminder from Rosenbach et al.(2008))

The starting periodic model of the MIL-47(V), built from its crystallographic data⁸, was first optimized by the density functional theory (DFT) method. Then, the partial charges for the atoms in this hybrid porous system were further extracted using the DFT calculation and Mulliken charge partitioning method as previously reported⁹. Based on the Accelrys DMol³ code¹⁰, both DFT calculations were performed by combining the PW91 GGA density functional¹¹ and the double numerical basis set containing polarisation functions on hydrogen atoms (DNP)¹². The resulting charges carried by all the atoms are reported in Table S1, where the detail locations of these atomic types on the framework are shown in Figure S4.

Table S1: Atomic partial charges carried by the MIL-47(V) framework atoms

Atoms	h_c	cg1	cg2	c_c	o_c	V	μ_2_o
Charges (e)	0.1463	-0.0709	-0.0679	0.6036	-0.496	1.207	-0.596

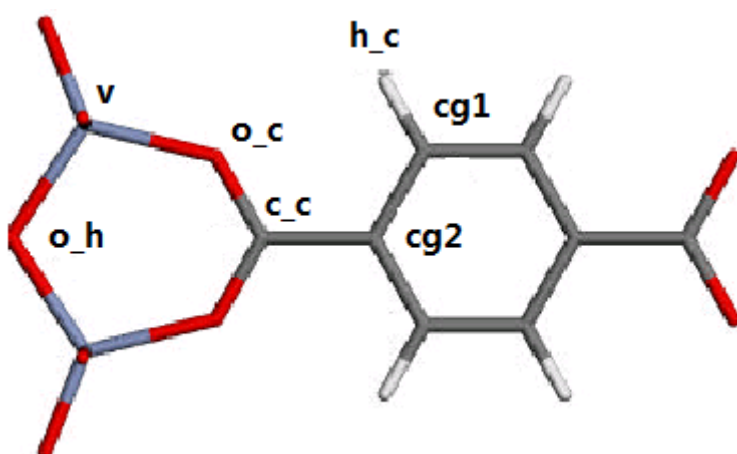


Figure S4 - Labels of the atoms for the organic and inorganic parts for MIL-47(V) materials corresponding to the force field atom types, to allow the easy reading of Tables S1 and S2.

4.2. Force field parameters used for MIL-47(V)

To study the mechanical response of the MIL-47(V) upon the external hydrostatic pressure, a new flexible force field has been derived for the MIL-47(V) starting with those previously reported for the MIL-53(Cr)¹³. In this force field, the intramolecular force constants for the organic moiety were

slightly adjusted from the widely used Consistent Valence Force Field (CVFF)¹⁴. The bond stretching, angle bending and torsion potentials are described by Eq. 1.

$$E_{ij}^{bond} = \frac{1}{2} k_{ij} (r_{ij} - r_0)^2 \quad (1)$$

$$E_{ijk}^{bending} = \frac{1}{2} k_{ijk} (\theta_{ijk} - \theta_0)^2$$

$$E_{ijkl}^{torsion} = k_{ijkl} [1 + \cos(n\phi_{ijkl} - \phi_0)]$$

where k_{ij} , k_{ijk} and k_{ijkl} are the force constants for the different interactions, r_{ij} the distance separating two atoms i and j , θ_{ijk} and θ_0 the angle involving three atoms i , j , k and the equilibrium angle respectively, n is the periodicity, ϕ the dihedral angle and ϕ_0 the factor phase.

A non-bonded Lennard-Jones (LJ) potential (Eq. 2) was used for describing the interactions between atoms of the organic linker. (See Table S2 for the corresponding parameters).

$$E_{ij}^{LJ} = 4\epsilon_{ij} \left[\left(\frac{\sigma_{ij}}{r_{ij}} \right)^{12} - \left(\frac{\sigma_{ij}}{r_{ij}} \right)^6 \right] \quad (2)$$

One can note that the parameters for o_c and o_h have been modified to reproduce accurately the distance between V and O atoms. The cross LJ parameters between the atoms with the different atomic types were obtained using the following Lorentz-Berthelot rule,

$$\epsilon_{ij} = \sqrt{\epsilon_{ii}\epsilon_{jj}} \quad \text{and} \quad \sigma_{ij} = \left(\frac{\sigma_{ii} + \sigma_{jj}}{2} \right) \quad (3)$$

<u>Bond potential</u>		
Bond Type	k_{ij} (kJ·mol ⁻¹ ·Å ⁻²)	r_0 (Å)
cg1-cg1	4015.045	1.34
cg1-cg2	4015.045	1.34
c_c-cg2	2943.723	1.47
c_c-o_c	4516.925	1.25
<u>Bending potential</u>		
Angle type	k_{ijk} (kJ·mol ⁻¹ ·rad ⁻²)	θ_0 (°)

cg1-cg2-cg1/ cg2-cg1-cg1	753.3034	120.0	
cg1-cg1-h_c / cg2-cg1-h_c	309.7182	120.0	
cg1-cg2-c_c	290.3186	120.0	
cg2-c_c-o_c	569.2484	120.0	
o_c-c_c-o_c	114.1649	123.0	
<i>Lennard-Jones potential</i>			
Atom type	σ_{ii} (Å)	ε_{ii} (kJ·mol ⁻¹)	
o_c	3.1200	0.2495	
c_c / cg1 / cg2	3.8068	0.2478	
h_c	2.4483	0.1602	
<i>Torsion potential</i>			
Dihedral type	k_{ijkl} (kJ·mol ⁻¹)	N	σ_0 (°)
cg2-cg1-cg1-cg2 / c_c-cg2-cg1-cg1 / cg2-cg1-cg1-h_c / h_c-cg1-cg1-h_c / c_c-cg2-cg1-h_c / h_c-cg1-cg2-cg1 / cg1-cg1-cg2-cg1 / cg1-cg2-c_c-o_c	2.0000 5.0000	2 2	180.0 180.0

Table S2 – Force field parameters for the intramolecular and non-bonded interactions of the organic moiety.

For the inorganic part, the potential parameters for the V-O bond stretching as well as the non-bonded LJ interaction of V atom were adopted from the universal force field (UFF). The parameters for the c_c-o_c-V three body interaction were considered to have the same values previously used for the c_c-o_c-Cr term in MIL-53(Cr)¹³. The torsion term between the inorganic and the organic parts, cg2-c_c-o_c-V, was adjusted by our own in order to capture accurately the key structural characteristics of the MIL-47(V) upon the hydrostatic pressure. It should be noted that the non-bonded interactions concern atoms separated by exactly three bonds usually described as 1-4 van der Waals interactions with LJ potentials.

<u>Bond potential</u>			
Bond Type	k_{ij} (kJ·mol ⁻¹ ·Å ⁻²)	r_0 (Å)	
V-o_c	2009.7041	1.95	
V-o_h	2009.7041	1.89	
<u>Bending potential</u>			
Angle type	k_{ijk} (kJ·mol ⁻¹ ·rad ⁻²)	θ_0 (°)	
c_c-o_c-V	115.8186	137.6	
<u>Lennard Jones potential</u>			
Atom type	σ_{ii} (Å)	ε_{ii} (kJ·mol ⁻¹)	
V	2.8010	0.0669	
o_h	3.1200	0.2495	
<u>Torsion potential</u>			
Dihedral type	k_{ijkl} (kJ·mol ⁻¹)	N	σ_0 (°)
cg2-c_c-o_c-V	18.0000	2	180.0

Table S3 – Force field parameters for the intramolecular and non-bonded interactions of the inorganic part.

4.3. Molecular Dynamics Simulations

All the molecular dynamics (MD) simulations were performed using the DL_POLY_2.20 program¹⁵ in the NσT ensemble to allow the change of both size and shape, using the Berendsen thermostat and barostat. The optimal relaxation times for the thermostat and the barostat were 1.0 ps and 5.0 ps respectively, which is a compromise between the simulation time and energy stability. A cutoff radius of 12.0 Å was applied to all the LJ interactions, and the long-range electrostatic interactions were handled using the Ewald summation technique. The SHAKE-RATTLE and the usual Velocity Verlet algorithms are used to constrain rigid bonds and to integrate the equations of motion¹⁵ respectively.

The initial configuration of MIL-47(V) was taken from its experimental single-crystal X-ray diffraction (XRD) data⁸. The MD simulations were performed at 300 K with a variety of pressures

up to 350 MPa. Further to calculate the hysteresis curve, the closed form obtained at 350 MPa was considered as the starting configuration and the simulations were conducted at various pressures down to 1 MPa. The simulation box consists of 32 unit cells for all the MD runs with a time step of 1 fs. Each simulation system was equilibrated with 1×10^6 steps (i.e. 1 ns) followed by 2×10^6 steps (i.e. 2 ns) for the production. Some testing runs with the longer simulation time (up to 10 ns) were also carried out and we found similar results.

4.4. Calculation of the vibrational frequencies using energy minimizations

Vibrational frequencies were further calculated to validate the force field developed in this work. These calculations were conducted using the GULP program¹⁶, and a correction value of -150 cm⁻¹ for the anharmonicity was used for the stretching and bending frequencies¹⁷. The vibrational frequencies of the carboxylate groups and the V-O bond were extracted from the calculation for the open form of MIL-47 (V) and further compared to the experimental data obtained by the infra-red spectroscopy¹⁸, as reported in Table S4. As can be seen from this table, the calculated frequencies are in good agreement with the experimental data, indicating the applicability of the current flexible force field.

	Experimental	Simulated
$\nu(\text{VO})$	902	954
$\nu(\text{Sym OCO})$	1400	1386
$\nu(\text{Antisym OCO})$	1543	1530

Table S4 – Simulated vibrational frequencies expressed in cm⁻¹ compared to the ones extracted by Infra-red spectroscopy¹⁸.

4.5. Evolution of the unit cell parameters of the MIL-47(V) structure as a function of the pressure

Figure S5 reports the MD simulated evolution of the unit cell parameters of the MIL-47(V) at 300 K.

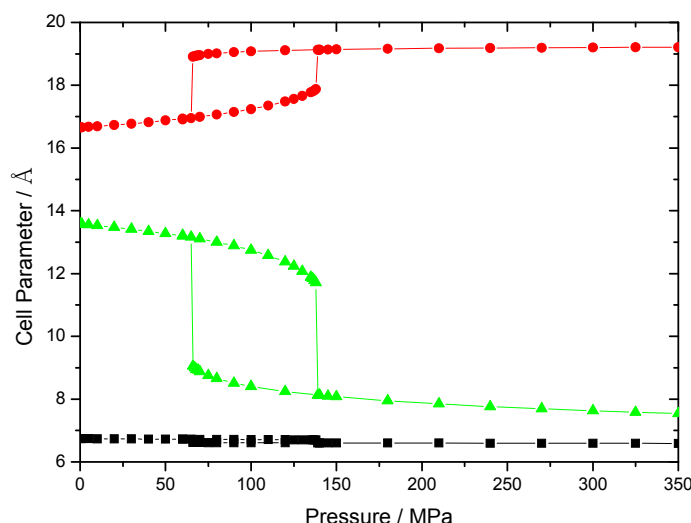


Figure S5 –Evolution of the unit cell parameters for MIL-47(V) as a function of the pressure at 300 K. The a , b and c parameters are shown as circles, triangles and squares respectively.

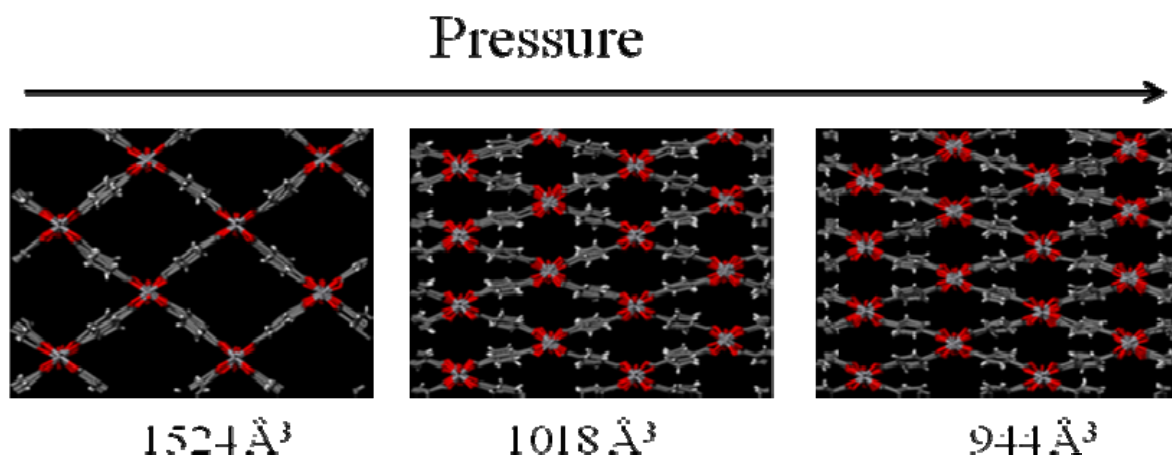


Figure S6 –Evolution of the crystal structure of MIL-47(V) upon the whole mechanical pressure range up to 350 MPa

The above three structures are provided as cif files with the labels: MIL-47(V)-Openform, MIL-47(V)-Closedform140MPa and MIL-47(V)-Closedform350MPa respectively.

4.6. Evolution of the energetics of MIL-47(V) during the breathing

Figures S7a and S7b report the evolution of the intra- and intermolecular energy contributions as a function of the MD simulation elapse time, evaluated starting from the open form at 140 MPa. As one can be observed, both the intramolecular terms including valence and dihedral angles, and the intermolecular van der Waals and electrostatic contributions, show a sudden changed when the structural transition occurs. The evolution of the total energy has been also traced from the open to the closed form as well as from the closed to the open form (Figure S8a and S8b) in order to estimate the activation barrier for both transitions.

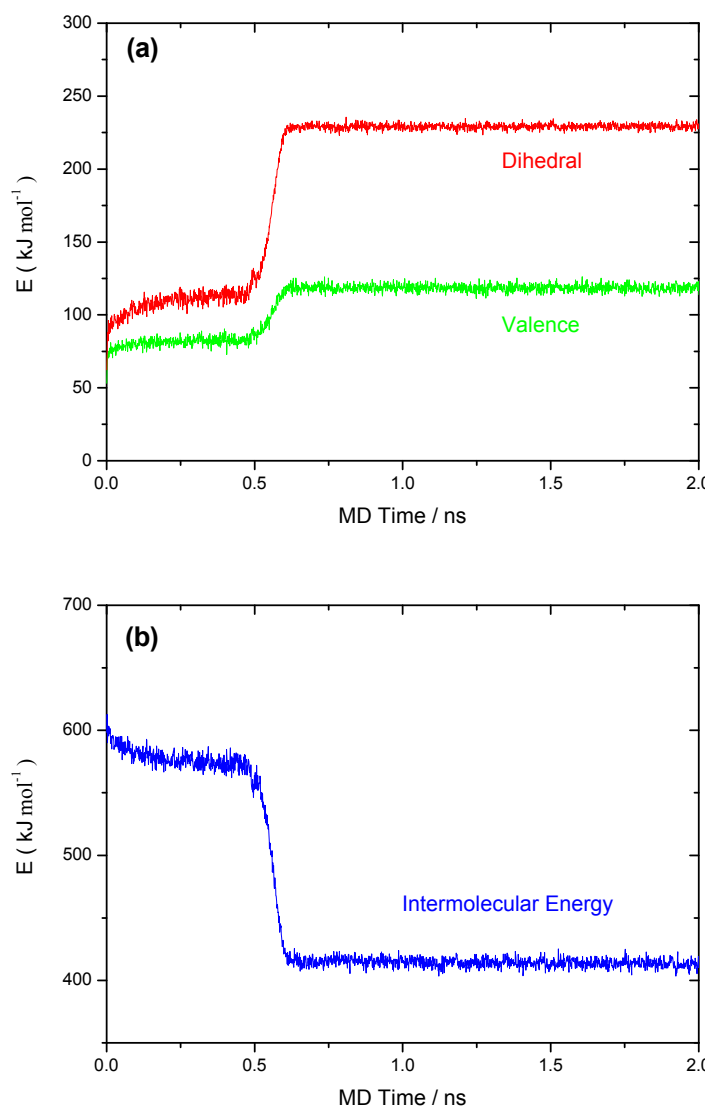


Figure S7 –Evolution of (a) the intramolecular (valence angles and dihedral angles) and (b) intermolecular (van der Waals and electrostatic) energies, as a function of the MD simulation time

starting with the open form structure at 140 MPa.

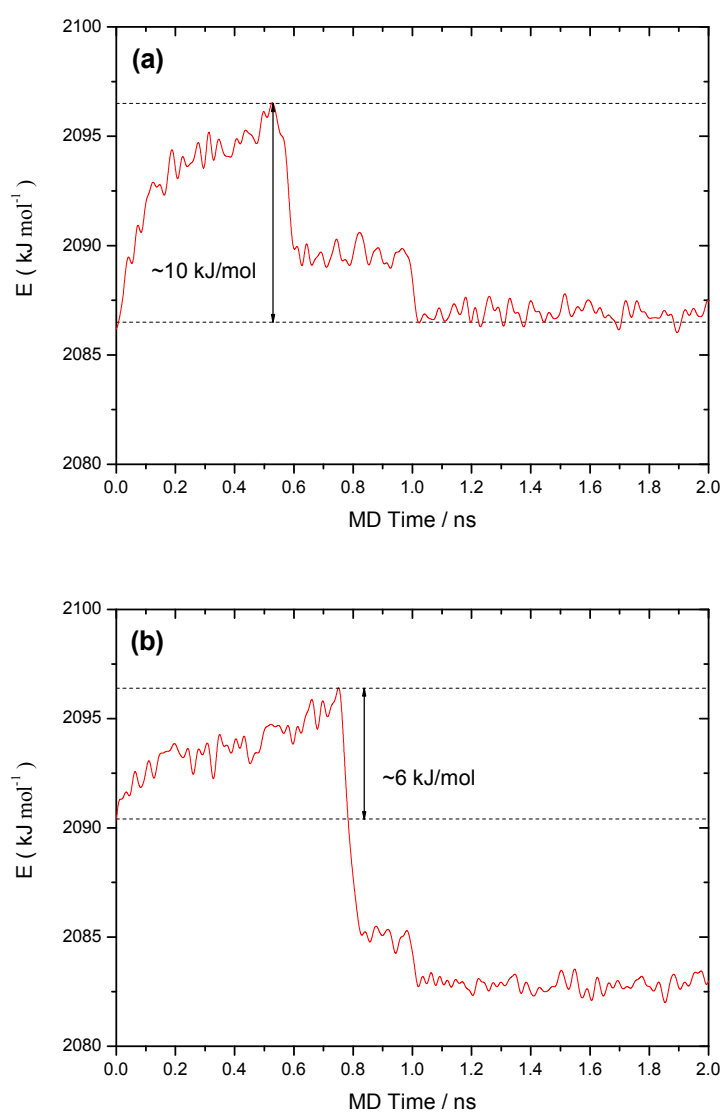


Figure S8 –Total energy plot for the transition from the open form to the closed form at 140 MPa (a) and the transition from the closed form to the open form at 65 MPa (b).

4.7. Distributions of the characteristic O-V-O valence angles and V-o_c-c_c-cg2 dihedral angles

Figure S9a and S9b show the distributions of the characteristic o-V-o valence angles (averaged from the o_c-V-o_c, o_c-V-o_h, and o_h-V-o_h angles) and V-o_c-c_c-cg2 dihedral angles for the open and closed pore forms.

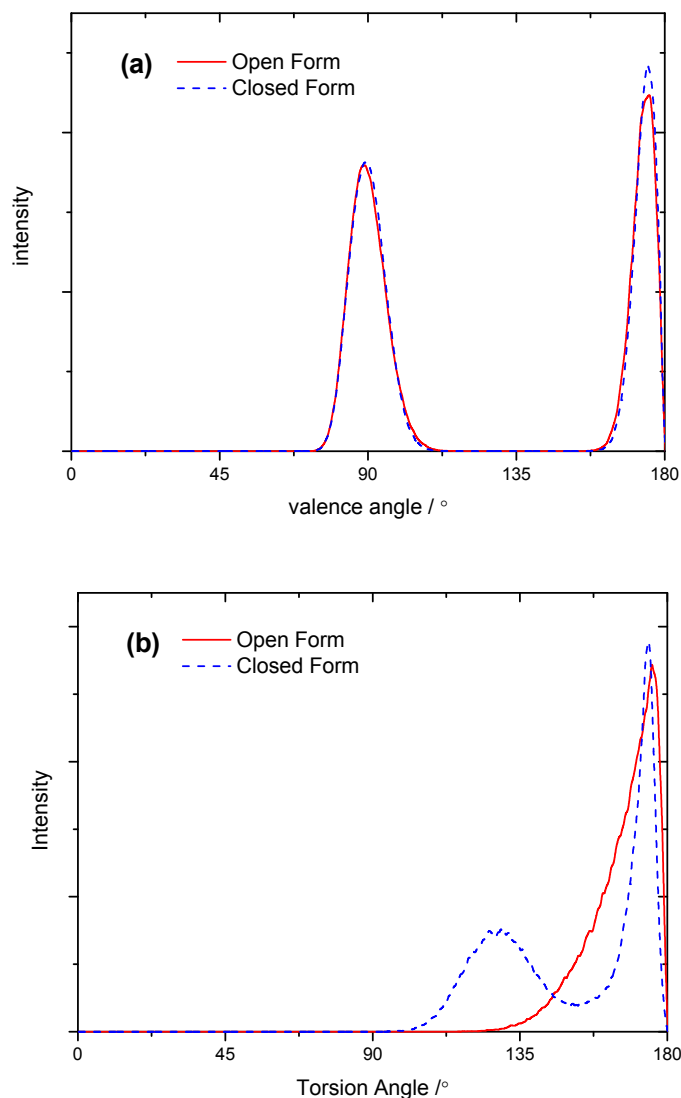


Figure S9 –Distributions of the characteristic O-V-O valence angles (a) and V-o_c-c_c-cg2 dihedral angle (b) for both the open and closed pore forms.

4.8. Plausible structure model for the MIL-47(V) at 340.1 MPa volume V= 866.6 Å³

The starting structural model was guessed from the anhydrous form of MIL-53(Fe) which shows very similar cell parameters than the MIL-47(V) structure observed at 340.1 MPa. This structure was thus geometrically optimized using the Forceite software¹⁰, by maintaining the fixed experimental unit cell parameters reported in Table 1 ($a=21.117\text{ \AA}$, $b=6.710\text{ \AA}$, $c=6.717\text{ \AA}$, $\beta=114.41^\circ$). To that purpose, the MIL-47(V) structure was treated using the force field described above while the electrostatic contributions were calculated using the partial charges described above. A cutoff radius of 12 Å was applied to the van der Waals interactions and the long-range electrostatic interactions were handled using the Ewald summation technique. The convergence criteria were defined to $2.0 \times 10^{-5}\text{ kcal/mol}$ (energy), $0.001\text{ kcal/(mol\cdot\AA)}$ (forces), and $1.0 \times 10^{-5}\text{ \AA}$ (displacement), respectively.

The resulting structure is provided as a cif file with the label MIL-47(V)340.1MPa. This structure was validated by a very good agreement between the XRD pattern calculated from this simulated structure and the experimental one (Figure S10).

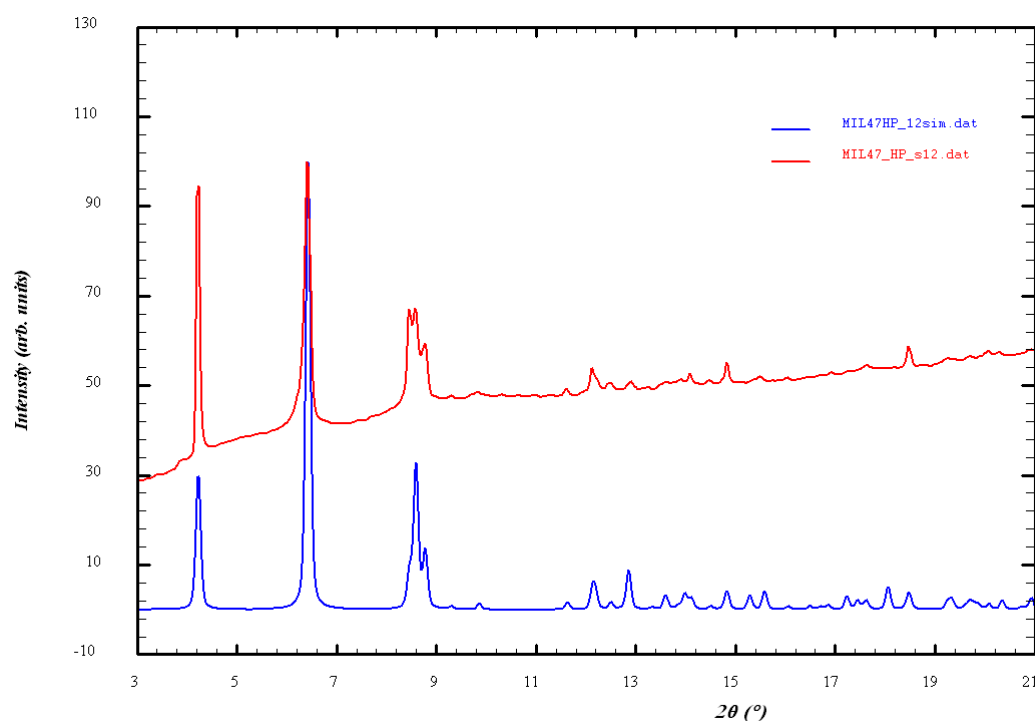


Figure S10 –Comparison between the X-ray diffraction pattern calculated from the simulated structure (in blue) labeled as (MIL-47(V)340.1MPa) and the experimental one (in red).

References

- [1] H. Giesche, *Part. Part. Syst. Charact.* **2006**, *23*, 9.
- [2] T. Woignier, F. Despetis, A. Alaoui, P. Etienne, J. Phalippou, *J. Sol-Gel Sci. Technol.* **2000**, *19*, 163.
- [3] I. Beurroies, M. Boulhout, P. L. Llewellyn, B. Kuchta, G. Férey, C. Serre, R. Denoyel, *Angew. Chem., Int. Ed.* **2010**, *49*, 7526.
- [4] A. P. Hammersley, S. O. Svensson, M. Hanfland, A. N. Fitch, and D. Häusermann, *High Press. Res.* **1996**, *14*, 235.
- [5] J. Rodriguez-Carvajal, A program for Rietveld refinement and pattern matching analysis. In Collected Abstracts of Powder Diffraction Meeting, 1990; pp 127.
- [6] T. Roisnel, J. Rodriguez-Carvajal, In Abstracts of the 7th European Powder Diffraction Conference, Barcelona, Spain, 2000; p 71.
- [7] H. K. Mao, J. Xu, P. M. Bell, *J. Geophys. Res.* **1986**, *91*, 4673.
- [8] K. Barthelet, J. Marrot, D. Riou, G. Férey, *Angew. Chem., Int. Ed.* **2002**, *41*, 281.
- [9] N.A. Ramsahye, G. Maurin, S. Bourrelly, P.L. Llewellyn, T. Loiseau, G. Férey, *Phys. Chem. Chem. Phys.* **2007**, *9*, 1059.
- [10] Accelrys Inc., San Diego, **1999**.
- [11] J.P. Perdew, Y. Wang, *Phys. Rev. B*, **1992**, *45*, 13244.
- [12] W.J. Hehre, J.H. Ditchfield, J.A. Pople, *J. Chem. Phys.*, **1972**, *56*, 2257.
- [13] F. Salles, A. Ghoufi, G. Maurin, R. G. Bell, C. Mellot-Draznieks, G. Férey, *Angew. Chem. Int. Ed.* **2008**, *47*, 8487.
- [14] P. Dauber-Osguthorpe, V.A Roberts, D. J. Dauber-Osguthorpe, J. Wolf, M. Genest, A.T. Hagler, *Proteins*, **1988**, *4*, 31.
- [15] W. Smith, T.R. Forester, *J. Mol. Graph.*, **1996**, *14*, 136.
- [16] J.D. Gale, *J. Chem. Soc. Faraday Trans.*, **1997**, *93*, 629.
- [17] D.W. Lewis, G. Sastre, *Chem. Commun.*, **1999**, 349.
- [18] L. Hamon, H. Leclerc, A. Ghoufi, L. Oliviero, A. Travert, J.C. Lavalle, T. Devic, C. Serre, G. Férey, G.D. Weireld, A. Vimont, G. Maurin, *J. Phys. Chem. C* **2011**, *115*, 2047.